



Enhanced molecular oxygen activation of Ni^{2+} -doped BiO_{2-x} nanosheets under UV, visible and near-infrared irradiation: Mechanism and DFT study

Jun Li^{a,b}, Jia Wang^{a,b}, Gaoke Zhang^{a,b,*}, Yuan Li^{a,b}, Kai Wang^{a,b}



^a Hubei Key Laboratory of Mineral Resources Processing and Environment, Hubei Provincial Collaborative Innovation Center for High Efficient Utilization of Vanadium Resources, School of Resources and Environmental Engineering, Wuhan University of Technology, 122 Luoshi Road, Wuhan 430070, China

^b State Key Laboratory of Silicate Materials for Architectures, Wuhan University of Technology, Wuhan 430070, China

ARTICLE INFO

Keywords:
 BiO_{2-x} nanosheet
Molecular oxygen activation
Doping
Near-infrared light
DFT calculations

ABSTRACT

Although molecular oxygen activation plays a significant role in photocatalytic process for pollutants removal, it is still challenging to activate molecular oxygen into superoxide radical ($\cdot\text{O}_2^-$) by photocatalysts under near-infrared (NIR) light irradiation. Herein, we successfully synthesized Ni^{2+} -doped BiO_{2-x} nanosheets, which could efficiently achieve the molecular oxygen activation into $\cdot\text{O}_2^-$ under ultraviolet (UV), visible and NIR irradiation. Meanwhile, we found the doping Ni^{2+} facilitated the formation of BiO_{2-x} nanosheets. More importantly, the contribution of doping Ni^{2+} on full spectrum molecular oxygen activation over Ni^{2+} -doped BiO_{2-x} was further confirmed by experiments and density functional theory (DFT) study. The introduction of Ni^{2+} into BiO_{2-x} structure resulted in the formation of a new doping energy level band between the valence band (VB) and conduction band (CB) of Ni^{2+} -doped BiO_{2-x} , which contributed to the faster separation of carriers and highly efficient full spectrum driven molecular oxygen activation under UV, visible and NIR irradiation, especially with the irradiation of NIR light as compared to BiO_{2-x} . In addition, the doping Ni^{2+} promoted the optical absorption property of BiO_{2-x} with narrowing band gap and the up-shift position of VB and CB. As expected, the Ni^{2+} -doped BiO_{2-x} nanosheets exhibited enhanced photocatalytic activity for rhodamine B (RhB) degradation under UV, visible and NIR irradiation than pure BiO_{2-x} nanosheets. The photocatalyst still revealed high photocatalytic activity even after five cycles. Finally, a possible photocatalytic mechanism of the degradation processes by Ni^{2+} -doped BiO_{2-x} was proposed. This work not only confirmed Ni^{2+} doping could promote the formation of BiO_{2-x} nanosheets and enhance their full spectrum driven molecular oxygen activation ability, but also presented an in-depth understanding on the mechanism of full spectrum driven molecular oxygen activation.

1. Introduction

Since TiO_2 was firstly reported for photocatalytic water splitting in 1972, the efficient utilization of solar energy for photocatalytic hydrogen evolution (PHE) and environment decontamination has been gained extensive attention due to the imminent energy dilemma and increasing pollution issues [1–13]. For improving the utilization efficiency of solar energy by photocatalysts, various strategies, such as doping [14–16], defect engineering [17,18], semiconductor recombination [19–23], dye sensitization [24,25], deposition of noble metals [26,27] and so on, have been developed. Especially, doping engineering has been developed and demonstrated to potentially improve the photocatalytic activity of catalysts, benefiting from the shorter diffusion lengths of photogenerated carriers in these doped materials, which could be to restrict or even eliminate photogenerated electron-hole pairs recombination. Stimulated by the doping

engineering, metal-doping [28,29] and nonmetal-doping [30,31] have been widely used to modify the electronic structure and consequently increase the light absorption range of photocatalysts for obtaining higher efficient visible-driven photocatalysts. Zhang et al. [32] reported that Zn doped Fe_3O_4 hollow submicrospheres improved the photo-Fenton activity for degradation of pollutants under visible light irradiation than pure Fe_3O_4 , which resulted from their hollow mesocrystal structure and Zn-doping. Xing et al. [33] reported that the doped Ni^{2+} and Ti^{3+} species could significantly narrow the band gap of anatase TiO_2 due to the formation of mid-gap states, hence this photocatalyst exhibited unprecedented higher photocatalytic activity than that of the pure TiO_2 and the Ni^{2+} doped TiO_2 . Zhong et al. [34] reported nitrogen-doped carbon consisted of abundant micropores and an ultra-high specific surface area (up to $2433 \text{ m}^2 \text{ g}^{-1}$), leading to high performances in electrocatalytic hydrogen evolution reaction (HER) and supercapacitors. Although doping strategies could vastly improve the

* Corresponding author at: State Key Laboratory of Silicate Materials for Architectures, Wuhan University of Technology, Wuhan 430070, China.
E-mail address: gkzhang@whut.edu.cn (G. Zhang).

utilization efficiency of solar energy, most photocatalysts couldn't achieve the utilization of NIR light due to their relatively larger band gaps.

For full utilization of solar energy, pioneer work has developed various up-conversion photocatalyst for water purification, such as phosphor coupled C-TiO₂, NaYF₄:Yb,Tm/CdS composite and BiErWO₆ [35–37]. Additionally, a few of NIR light direct responsive photocatalysts have also been reported to improve the utilization efficiency of solar energy [38–41]. Especially, the full spectrum responsive photocatalysts, such as Bi₂MO₆ (M=W, Mo) [42], Cu₂(OH)PO₄ [43], Ag₂O [44] and TiO₂/Bi₂WO₆ [45], which exhibited satisfactory photocatalytic activity for degradation of pollutants. The highly efficient NIR light responsive photocatalysts for degrading organic pollutants still need to be further developed. Recently, Bi-based compounds have caught much attention as its narrow band gap and better photocatalytic performance under visible light irradiation due to the hybridized O 2p and Bi 6s² valence bands [46]. The majority of two-dimensional (2D) Bi-based photocatalysts are UV-vis light responsive photocatalysts, such as Bi₂SiO₅ [47], Bi₂MoO₆ [48], Bi₂O₂CO₃ [49], BiOX (X=Cl, Br, I) [50,51] and so on. However, full spectrum responsive 2D Bi-based photocatalysts with high photocatalytic performance, especially which could activate O₂ into ·O₂[−] under NIR light irradiation, have been rarely reported.

Herein, based on the doping engineering, we designed and synthesized the highly efficient full spectrum responsive 2D Ni²⁺-doped BiO_{2-x} nanosheets via a facial hydrothermal method. The experimental results demonstrated doping Ni²⁺ could promote the formation of BiO_{2-x}. Meanwhile, DFT calculations confirmed the introduction of Ni²⁺ into BiO_{2-x} structure resulted in the formation of a new doping energy level band between VB and CB of Ni²⁺-doped BiO_{2-x}, attributing to the hybridization of d-orbital of Ni atoms and p-orbital of O atoms. What's more, the introducing Ni²⁺ could accumulate charge on oxygen molecule adsorbed on BiO_{2-x}. The effective capture of electrons by O₂ could restrain the recombination of photoinduced carriers and enhance full spectrum driven molecular oxygen activation ability of Ni²⁺-doped BiO_{2-x}, especially in the NIR region, contributing to the enhanced RhB photocatalytic oxidation activity than pure BiO_{2-x} nanosheets. Comprehensive study of this Ni²⁺-doped BiO_{2-x} material by diffraction, spectroscopy, microscopy analyses reveals that Ni²⁺ ions was successfully introduced into BiO_{2-x} structure. Besides, the molecular oxygen activation mechanism of Ni²⁺-doped BiO_{2-x} by the standpoint of potentials of CB, charge distribution and theoretical calculations was explored.

2. Experimental

2.1. Materials

Sodium bismuthate oxide (NaBiO₃), sodium hydroxide (NaOH) and nickel nitrate hexahydrate (Ni(NO₃)₂·6H₂O) were purchased from Alfa or Sinopharm Chemical Reagent Co., Ltd., Shanghai, China. All the reagents are analytical grade and used without further purification.

2.2. Photocatalyst preparation

2.2.1. Synthesis of BiO_{2-x}

Synthesis of BiO_{2-x} is the same as our reported work [52]. In a typical synthesis, 2.4 g NaOH and 2.8 g NaBiO₃ were added into 60 mL of deionized water with magnetic stirring. After stirring for 30 min, the suspension was transferred into stainless steel PVP-lined autoclave of 90 mL capacity. The autoclave was sealed and heated at 180 °C for 18 h, and then cooled to room temperature naturally. The final products were collected by centrifugation, washed with distilled water and dried at 80 °C for 4 h.

2.2.2. Synthesis of Ni²⁺-doped BiO_{2-x}

In a typical synthesis, NaBiO₃, Ni(NO₃)₂·6H₂O and NaOH were added into 60 mL of deionized water under magnetic stirring with Bi and Ni molar ratios of 10:0.2, 10:0.4, 10:0.6 and 10:0.8, which were marked by 2%NBO, 4%NBO, 6%NBO and 8%NBO, respectively. After stirring for 60 min, the suspension was transferred into stainless steel PVP-lined autoclave of 90 mL capacity. The autoclave was sealed and heated at 180 °C for 6 h and then cooled to room temperature naturally. The final products were collected by centrifugation, washed with distilled water and dried at 80 °C for 4 h.

2.3. Characterization

The structure and crystallinity of the as-prepared samples were determined by X-ray diffraction (XRD) analysis on a D/MAX-RB diffractometer under the operation conditions of 40 kV and 50 mA. The optical properties were measured using a spectrophotometer (Lambda 750 S), giving an output of transmittance in the UV, visible, and infrared ranges (200–2500 nm). X-ray photoelectron spectra (XPS) were measured using a PHI Quantera II system to study the value states, energy spectrum, the valence band and so on. Binding energies were referred to the C 1 s peak at 284.5 eV of the surface adventitious carbon. The electronic spin resonance (ESR) spectrum was recorded on an electron paramagnetic resonance (EPR) spectrometer (A300-10/12, Bruker) to further detect the presence of oxygen vacancy as well as ·OH and ·O₂[−] radicals in the photocatalytic reaction system with 5,5-dimethyl-1-pyrroline Noxide (DMPO: 50 mM, 0.2 mL) in the aqueous with suspended photocatalyst under UV, visible and NIR irradiation. Field emission scanning electron microscope (FESEM, Hitachi SU8010, Japan) was used to observe the morphology.

The calculations were implemented using the Vienna Ab-initio Simulation Package (VASP) with a plane-wave cutoff energy of 400 eV. A (2 × 2) supercell was used to simulate the crystal structure of BiO_{2-x} and Ni²⁺-doped BiO_{2-x}. During the optimizations, the energy and force converged to 10^{−5} eV/atom and 0.02 eV/Å, respectively.

2.4. Photocatalytic activity evaluation

2.4.1. UV and visible light responsive photocatalytic activity

For exploring the photocatalytic performance of the as-synthesized Ni²⁺-doped BiO_{2-x} nanosheets, the RhB was chosen as the targeted contaminant to evaluate the photocatalytic activity under UV, visible and NIR irradiation. 0.1 g of the as-prepared products was added into 100 mL of RhB in aqueous solution (10 mg/L). The suspensions were irradiated with UV or visible light after the mixed suspensions were constantly stirred for 0.5 h in the dark to disperse the catalyst. The 100 W LED lamps with the wavelengths of 365 and 420 nm were as the UV and visible light sources. At set time for 30 min, the homogeneous suspensions were measured for 6 mL that was analyzed by employing a UV-vis spectrophotometer (ORION AquaMate 8000, China) at its maximum absorption wavelength of 554 nm.

2.4.2. NIR light responsive photocatalytic activity

0.1 g of the as-prepared products was added into 100 mL of RhB in aqueous solution (10 mg/L). To eliminate the effect of the adsorption, the mixed suspensions were constantly stirred for 1 h in the dark to reach adsorption equilibrium. Moreover, the suspensions were irradiated with NIR light. The 100 W LED lamp with the wavelength of 770–860 nm was as the NIR light source. At set time for 1 h, the homogeneous suspensions were measured for 6 mL that was analyzed by employing a UV-vis spectrophotometer (Orion AquaMate 8000, China) at its maximum absorption wavelength of 554 nm.

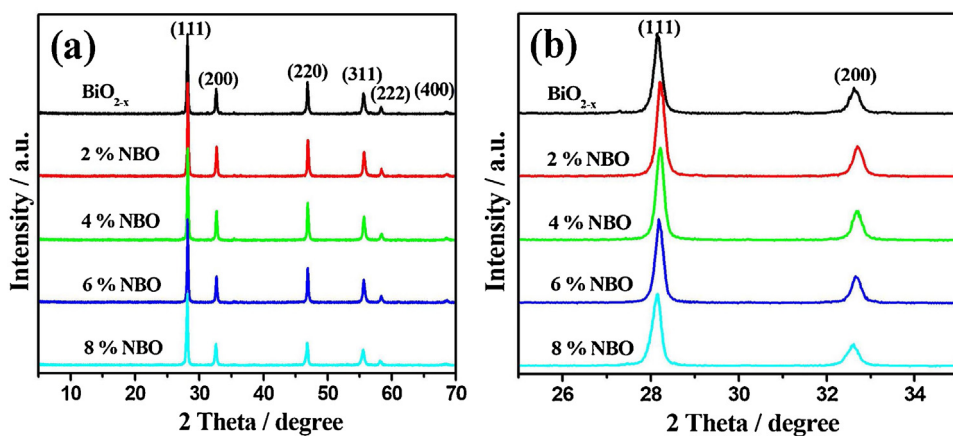


Fig. 1. (a) XRD patterns of as-prepared BiO_{2-x} , $x\%$ NBO ($x = 2, 4, 6, 8$). (b) The magnified view of (a) from 25° to 35° .

3. Results and discussion

3.1. Crystal structure

The crystal structures of the as-prepared samples were investigated by the XRD method. Fig. 1(a) shows the XRD patterns of BiO_{2-x} and Ni^{2+} -doped BiO_{2-x} in the range of 20 – 80° . The XRD pattern of BiO_{2-x} could be indexed to the cubic phase of BiO_{2-x} (JCPDS No. 47-1057). The XRD patterns of Ni^{2+} -doped BiO_{2-x} with different content of Ni^{2+} are matched well with cubic phase of BiO_{2-x} and no other peaks are observed, indicating the good distribution of Ni^{2+} doped in the BiO_{2-x} structure. It can be observed that the peaks of Ni^{2+} -doped BiO_{2-x} corresponding to the (111) and (200) plane shift slightly to higher 2θ , which could be ascribed to the electrostatic function of crystal facets and the action of Ni^{2+} [53]. Based on the Bragg's law, $d_{(h k l)} = n\lambda / (2\sin\theta)$, $d_{(h k l)}$ is the distance between crystal planes of $(h k l)$, λ is the X-ray wavelength and θ is the diffraction angle of the crystal plane $(h k l)$, the observed shift of the diffraction peaks to a higher angle directly reflects the diminution of interplanar spacing of 4%NBO [48,54], which results from the substitution of Bi ions with larger ion radius by the Ni^{2+} with smaller one. No characteristic peaks of other impurities are observed, indicating the high purity of the samples.

3.2. Full spectrum responsive photocatalytic activity and stability evaluation

The full spectrum responsive photocatalytic activity of the as-prepared samples for degradation of RhB in aqueous solution was evaluated under UV light ($\lambda = 365 \text{ nm}$), visible light ($\lambda = 420 \text{ nm}$) and NIR light ($770 < \lambda < 860 \text{ nm}$) irradiation, respectively. Before conducting the photocatalytic degradation experiments, the adsorption experiment in the dark has been carried out, showing that the adsorption equilibrium could be reached after 8 h (Fig. S1(a)). Fig. 2(a) reveals that Ni^{2+} doped BiO_{2-x} samples possess good photocatalytic property for degradation of RhB in aqueous solution under NIR light irradiation. When the content of Ni^{2+} doped in BiO_{2-x} structure was equal to 0.4 mmol, the Ni^{2+} doped BiO_{2-x} revealed the superior photocatalytic activity and exhibited 85% degradation ratio for RhB, which is better than BiO_{2-x} nanosheets under NIR light irradiation. Fig. S1(b) illustrates the superior photocatalytic degradation rate of RhB in aqueous solution by 4%NBO (0.24169 h^{-1}), which is higher than that by BiO_{2-x} (0.13357 h^{-1}), 2%NBO (0.15461 h^{-1}), 6%NBO (0.12945 h^{-1}) and 8%NBO (0.10539 h^{-1}) under NIR light irradiation. Meanwhile, 4%NBO nanosheets showed the degradation efficiencies of 100% for RhB in aqueous solution under either UV or visible light irradiation (Fig. 2(b)). In addition, 4%NBO nanosheets showed enhanced photocatalytic activity for degradation of RhB under either UV or visible light irradiation as compared to BiO_{2-x} nanosheets (Fig. 2(c,d)). The

degradation rate k of RhB in aqueous solution degradation under UV and visible lights irradiation by BiO_{2-x} and 4%NBO was also evaluated. The degradation rate k of RhB in aqueous solution with the presence of 4%NBO is much higher than that by pure BiO_{2-x} under either UV or visible light irradiation (Fig. S1(c,d)). Hence, it can be concluded that the photocatalytic activities of BiO_{2-x} nanosheets under UV, visible and NIR irradiation could be obviously improved by Ni^{2+} doping.

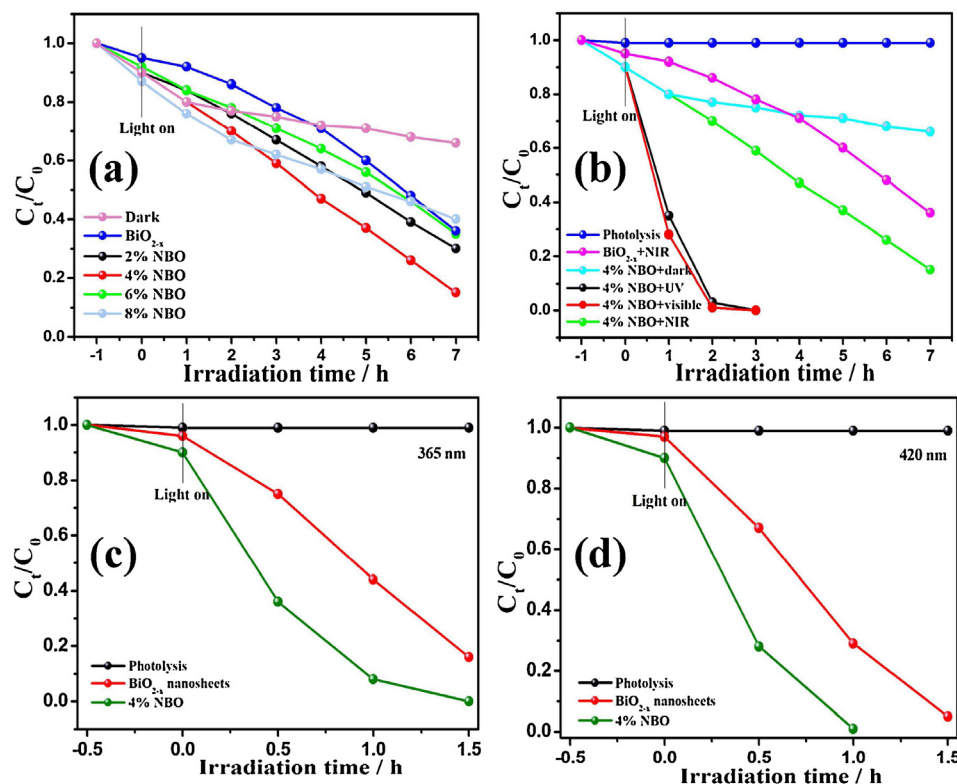
As the stability of photocatalysts is a general requirement for the practical application, the reusability of the 4%NBO for photocatalytic degradation of RhB in aqueous solution was studied and the results are given in Fig. 3. During every cycling experiment, the residual photocatalysis was collected, washed and finally dried at 80°C for 4 h for the next cycling run under the same conditions. After 5 cycles, 4%NBO still remained high photocatalytic performance (Fig. 3(a)) and the decrease of the degradation ratio of RhB by the 4%NBO catalyst can be attributed to the loss of the catalyst in the recovered process. Figs. 3(b) and S2 illustrate that the XRD patterns of 4%NBO before and after being utilized are almost the same, confirming that the photocatalyst possesses good stability.

3.3. Morphology characterization

Above results show that the content of Ni^{2+} in BiO_{2-x} structure can affect the photocatalytic activity of BiO_{2-x} , moreover, the 4%NBO reveals the optimal photocatalytic performance. Therefore, 4%NBO was chosen to study the morphology, optical and chemical structure properties. The morphology of the as-prepared 4%NBO was characterized by FESEM and TEM. Fig. S3 shows the typical nanosheet morphology of 4%NBO nanostructure. Fig. 4(a) reveals the appearance of hexagon with the clear border. High resolution TEM (HRTEM) images provide further insight into the microstructure of the 4%NBO nanosheet. The lattice fringes of the 4%NBO could be clearly seen in Fig. 4(b), the well-defined lattice interplanar spacing of about 0.317 nm could be attributed to the distances of (111) plane of BiO_{2-x} . Irregular holes with sizes ranging from several angstroms (\AA) to a few nanometers and disordered lattice were also presented in 4%NBO nanosheets, indicating the presence of numerous vacancies. For further studying the chemical composition of 4%NBO nanosheet, the EDS-mapping was used to analyze its element distribution, confirming 4%NBO nanosheets are composed of Ni, Bi and O elements (Fig. 4(c–f)). It is apparently that the doped Ni ions are distributed in the 4%NBO structure uniformly, demonstrating Ni^{2+} ions have successfully been doped into the BiO_{2-x} structure.

3.4. Composition and chemical state analysis

As shown in Fig. 5(a), it could be clearly seen that BiO_{2-x} and 4%NBO are composed of Bi, O and Ni, O, respectively. The XPS peaks of



Bi 4f_{7/2} (or Bi 4f_{5/2}) could be deconvoluted into two peaks with binding energy at 157.9, 163.2 and 158.5, 163.9 eV, which could be ascribable to Bi³⁺ and Bi⁵⁺ (Fig. 5(b)) [52,55], respectively. Furthermore, based on the quantitative results of the XPS spectrum of BiO_{2-x}, the molar ratio of Bi³⁺ to Bi⁵⁺ on the surface of BiO_{2-x} is 0.98, which is close to the theoretical value (1:1) and that of 4%NBO is calculated to be 1.02. The increasing ratio of Bi³⁺ to Bi⁵⁺ after the Ni²⁺ doping is due to incorporation of Ni²⁺ ions into the crystal structure. The result further proves that the Ni²⁺ has been successfully doped into BiO_{2-x} structure [56]. As depicted in Fig. 5(c), the binding energies of Ni 2p_{3/2} and Ni 2p_{1/2} are determined at 855.2, 861.3, 873.2 and 880.5 eV, typically attributed to the presence of Ni²⁺ [57–59], revealing Ni²⁺ ions exist in the BiO_{2-x} structure. In the experiment, the content of Ni²⁺ in BiO_{2-x} structure was adjusted to explore the effect of Ni²⁺ on the photocatalytic activity of BiO_{2-x} for degradation of RhB in aqueous solution, the Ni 2p high-resolution of 2%NBO and 6%NBO were also given (Fig. S4). To demonstrate the homogeneous doping of Ni element, the XPS

analysis of the sample was carried out after it was etched using argon ion (Table 1, Fig. S5). The result shows that the contents of the Ni element in the sample are almost invariant after etching 60 and 200 s, indicating homogeneous distribution of Ni element in 4%NBO structure. The peaks of O 1s high-resolution spectrum located at 528.8, 529.4 and 531.0 eV could be assigned to the lattice oxygen (Bi-O), chemical adsorbed oxygen [60] and oxygen vacancy [61], respectively (Fig. 5(d)). The XPS results demonstrate that Ni²⁺ was successfully doped into BiO_{2-x}, which may result in distinct optical and photoelectrochemical properties.

3.5. Optical properties

It is acknowledged that the metal doping could strongly affect the band structure of semiconductors with increased CB potential, which further affects their photocatalytic activity. As depicted in Fig. 6(a), both BiO_{2-x} and 4%NBO have strong absorption from UV, visible to NIR

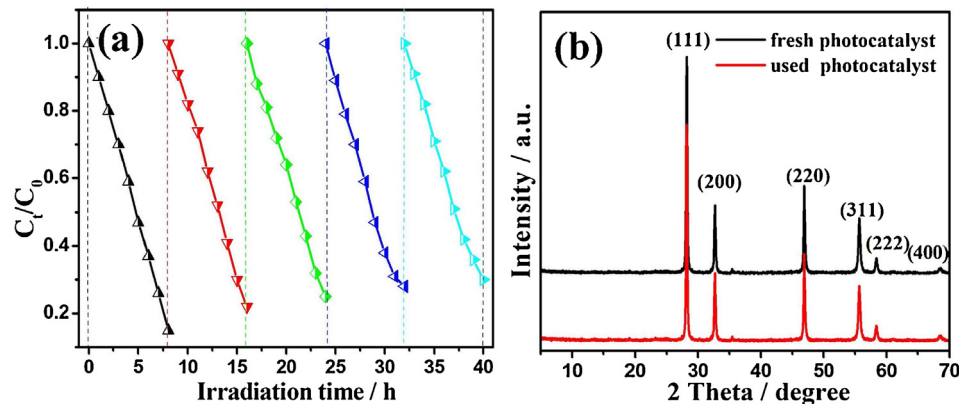


Fig. 3. (a) Photocatalytic degradation of RhB over 4%NBO during cycling operation with exposure to NIR light. (b) XRD patterns of 4%NBO samples before and after the photocatalytic degradation of RhB in aqueous solution.

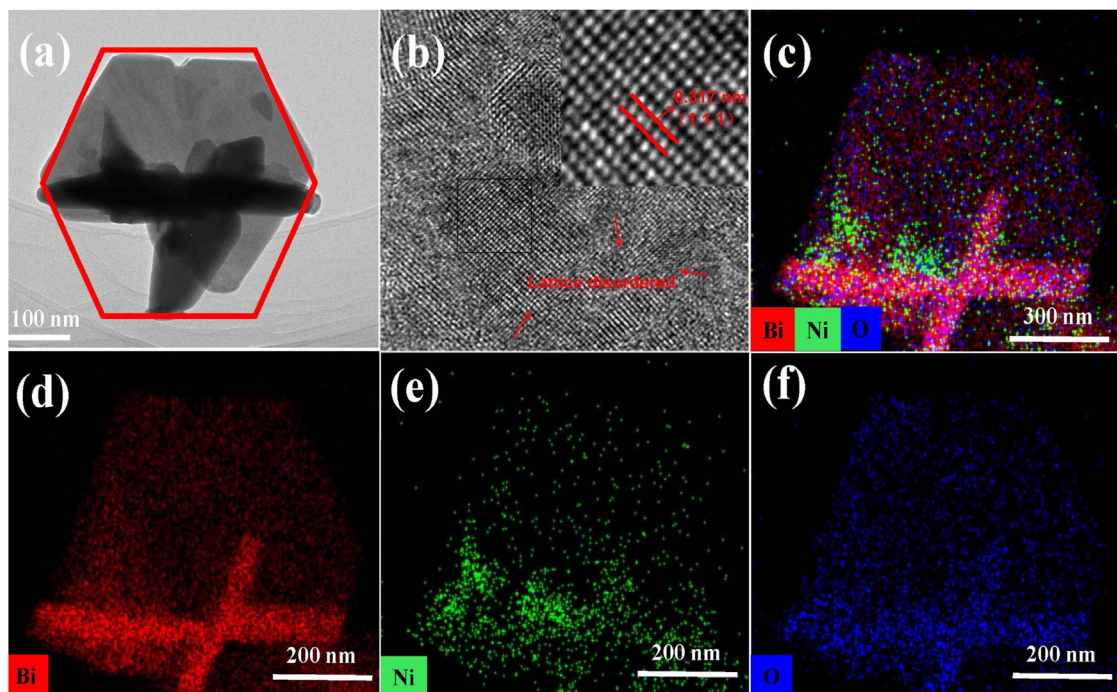


Fig. 4. (a) TEM image, (b) high-resolution TEM image and (c–f) elemental EDS-mapping images of 4%NBO nanosheets.

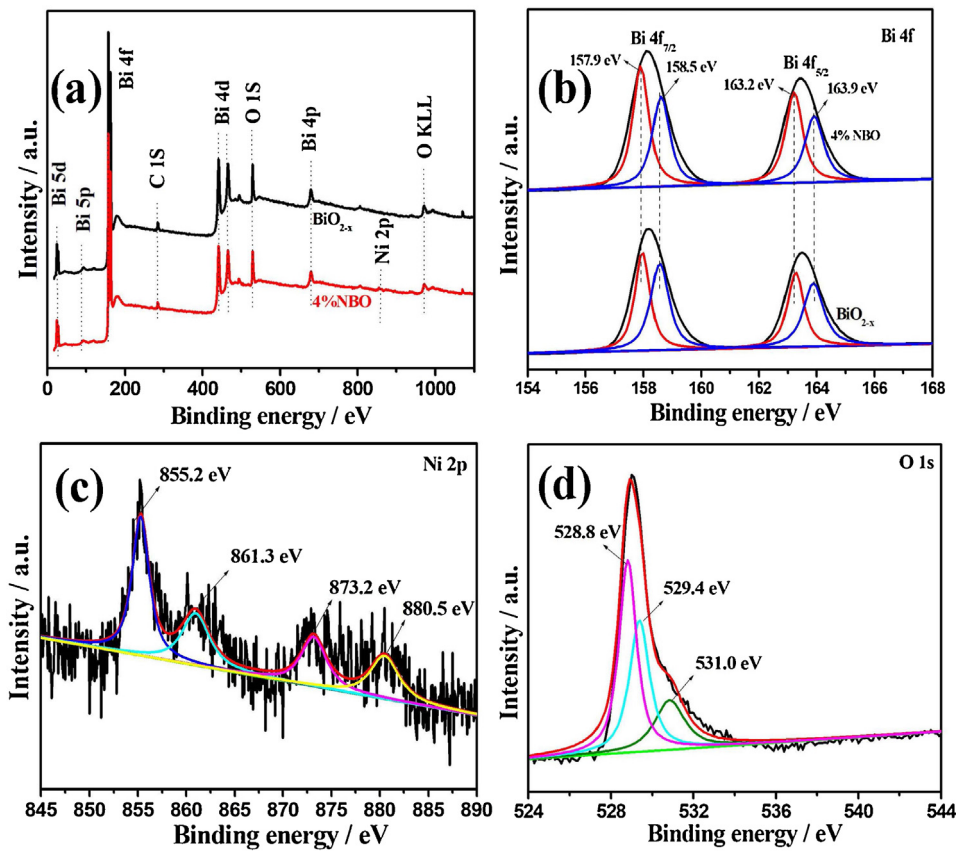


Fig. 5. XPS spectra of BiO_{2-x} and 4%NBO. (a) Wide survey spectra of BiO_{2-x} and 4%NBO. (b) Bi 4f high-resolution spectra of BiO_{2-x} and 4%NBO. (c) Ni 2p high-resolution spectrum of 4%NBO. (d) O 1s high-resolution spectrum of 4%NBO.

Table 1

The content of Bi, Ni and O elements in 4%NBO with different etching time.

sample	Content (Atomic %)			
	Bi	Ni	O	C
4% NBO (0 s)	15.82	1.51	46.61	36.06
4% NBO (60 s)	23.23	2.15	51.77	22.85
4% NBO (200 s)	26.60	2.14	55.34	15.92

light at the range of 200–2500 nm [52]. Doping Ni^{2+} alters the light absorption properties with red-shifting from 850 to 885 nm. Beyond that, the optical band gaps of BiO_{2-x} and 4%NBO could be determined by the follow equation [52,62,63]:

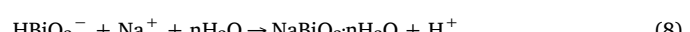
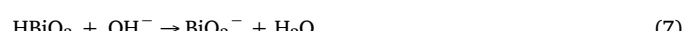
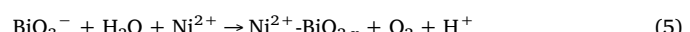
$$E_g = 1240/\lambda_{\max} \quad (1)$$

Where E_g represents band gap energy, and λ_{\max} is the biggest absorption edge of the samples. The band gaps of BiO_{2-x} and 4%NBO are estimated to be about 1.46 and 1.40 eV, respectively. On the basis of our previous work, the VB position of pure BiO_{2-x} was 0.95 eV and that of 4%NBO is measured by XPS valence spectra and the results are shown in Fig. 6(b) [52]. The VB position of 4%NBO is calculated to be approximate 0.87 eV. According to the optical absorption spectra, the corresponding CB minimum of BiO_{2-x} and 4%NBO could be located at -0.51 and -0.53 eV, respectively. Therefore, the introducing Ni^{2+} decreases the band gap value of BiO_{2-x} with the up-shift position of VB and CB, and the Ni^{2+} -doped BiO_{2-x} is much easier to be activated by UV, visible and NIR light.

3.6. The effect of Ni^{2+} on the formation of BiO_{2-x}

For exploring the formation mechanism of Ni^{2+} -doped BiO_{2-x} , the controlled condition experiments were carried out. Fig. 7(a) reveals the samples obtained in different reaction time with the addition of Ni^{2+} source, proving that the objective products can be successfully obtained when the reaction time is 2 h at 180 °C. As shown in Fig. 7(b), the pure BiO_{2-x} couldn't be synthesized within 6 h and the samples always contain the impurity phase without Ni^{2+} source, such as $\text{NaBiO}_3 \cdot n\text{H}_2\text{O}$. However, the pure samples could be easily obtained within 2 h with the addition of Ni^{2+} source in the experiment. Therefore, we conclude that the introduction of Ni^{2+} source could reduce the reaction barrier and facilitate the formation of BiO_{2-x} , displaying the Ni^{2+} -doped BiO_{2-x} is more stable than BiO_{2-x} [64,65]. Although the concentration of NaOH is more than 3 mol/L, we still couldn't get the pure target products and they are still with some impurities, such as Bi_4O_7 and $\text{NaBiO}_3 \cdot n\text{H}_2\text{O}$ with the absence of Ni^{2+} source. Thus, the Ni^{2+} ions play a vital role in the formation process of BiO_{2-x} nanosheets and the forming mechanism of Ni^{2+} -doped BiO_{2-x} could be mainly summarized as follows and

depicted in Fig. 7(c) according to the above analyses:

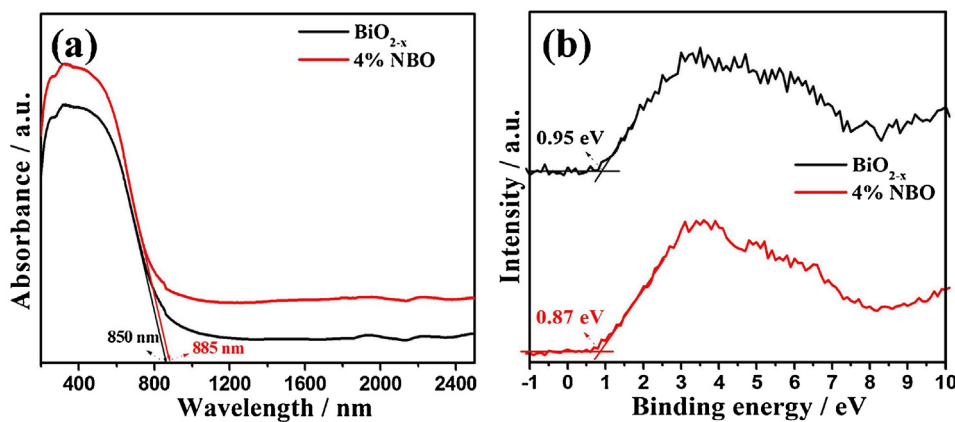


3.7. Oxygen vacancy analysis

Furthermore, to investigate possible photocatalytic mechanism, EPR spectra of the as-prepared samples were given in Fig. S6. BiO_{2-x} and 4% NBO show an obvious signal at g-value of 2.0, suggesting the presence of OVs in their structures [54,66,67]. The Raman spectrum of BiO_{2-x} and 4%NBO were also given in Fig. 8(a). Four strong vibrational peaks at 139, 309, 480 and 615 cm^{-1} could be clearly identified, which is in accordance with the Raman characteristic peaks of bismuth oxide [68]. Fig. 8(b) shows that the enlarged Raman spectra of BiO_{2-x} and 4%NBO at the range of 105–200 cm^{-1} . The vibration peak about 136 cm^{-1} moves slightly, suggesting Ni^{2+} has successfully been doped into BiO_{2-x} structure.

3.8. Photoelectrochemical and photoluminescence properties

The current response of the samples with respect to AC voltage as a function of frequency was measured by electrochemical impedance spectroscopy (EIS) to present the electrochemical interfacial reactions. Fig. 9(a) showed the Nyquist plots of the photocatalysts under dark conditions. In the Nyquist plot, a semicircle at high frequency is on behalf of the charge-transfer process, and the diameter of the semicircle represents the charge-transfer resistance [69,70]. Obviously, the diameter of the arc on the Nyquist plots is reduced after doping Ni^{2+} , suggesting doping Ni^{2+} ions not only increase charge transport but also lower the recombination ratio of electron-hole pairs. Photoluminescence (PL) is also another effective way to check the charge separation ability of the samples and generally lower intensity of the emission peak means lower separation ability for charge carriers. Fig. 9(b-d) presented the room temperature PL spectra of the BiO_{2-x} and 4%NBO. It could be clearly seen that the PL spectra reveal three emission peaks at around 368, 470 and 735 nm corresponding to the UV, visible and NIR light region, respectively, indicating the existence of latent defects in the structure of BiO_{2-x} and Ni^{2+} doped BiO_{2-x} [71].

Fig. 6. (a) The optical absorption spectra and (b) VB XPS spectra of BiO_{2-x} and 4%NBO.

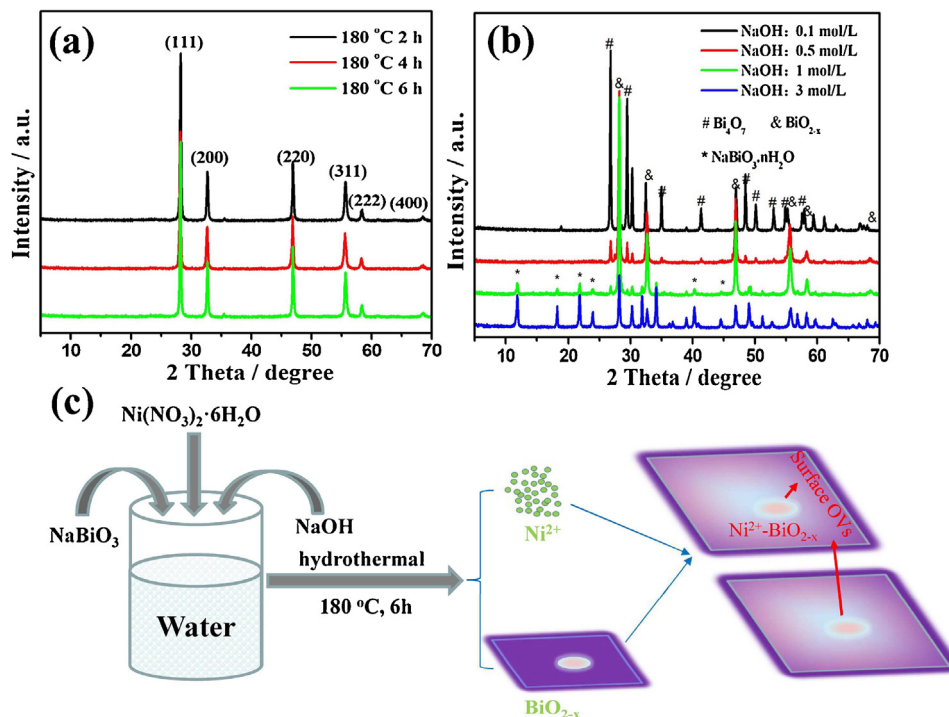


Fig. 7. XRD patterns of different controlled conditions: (a) Different prepared time in the existence of Ni source. (b) Different concentrations of NaOH at 180 °C and 4 h with the addition of Ni²⁺ source. (c) The forming schematic diagram of Ni²⁺-doped BiO_{2-x}.

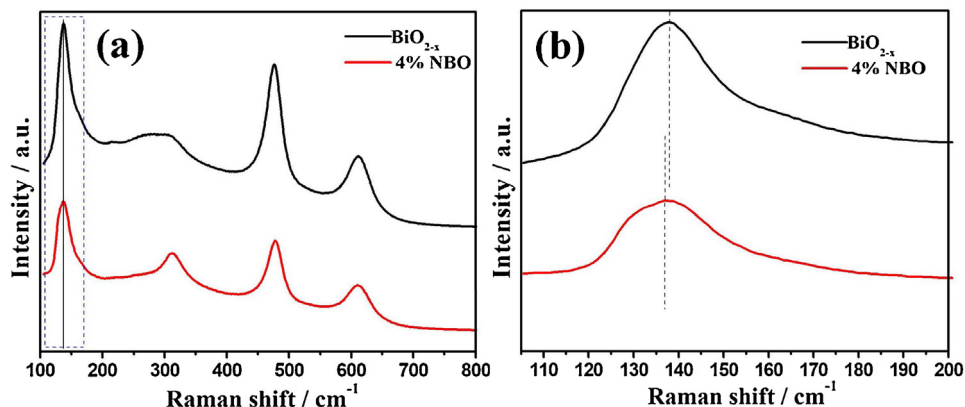


Fig. 8. (a) Raman spectra of BiO_{2-x} and 4%NBO. (b) The magnified view of (a) from 105 to 200 cm⁻¹.

Moreover, the intensity of PL spectrum of BiO_{2-x} decreased by introducing Ni²⁺, indicating that the modified BiO_{2-x} by Ni²⁺ can effectively restrain the carrier recombination. The doping Ni²⁺ in the structure of BiO_{2-x} can produce isolated states in the forbidden gap and act as electron acceptor to accelerate the separation of photogenerated electrons and holes, which has been confirmed by the following DFT calculations. The favorable conditions can contribute to the enhanced photocatalytic performance of Ni²⁺ doped BiO_{2-x}.

3.9. Identification of reactive species

As we all know, hydroxyl radical (·OH), superoxide radical (·O₂[−]) and hole (h⁺) are the uppermost active radical species in the process of photocatalytic degradation of organic pollutants. Isopropyl alcohol (IPA), sodium oxalate (Na₂C₂O₄) and benzoquinone (BQ) are usually used to the scavengers of ·OH, h⁺ and ·O₂[−], respectively [16,72–74]. Fig. 10(a) shows that when 0.2 mmol/L Na₂C₂O₄ or BQ is as a scavenger for h⁺ or ·O₂[−] in the system, the photo-degradation ratio of 4%NBO

decreases dramatically, demonstrating that h⁺ and ·O₂[−] are the dominant reactive species in the reaction process, while with the addition of IPA, the degradation ratio of 4%NBO declines slightly, proving that ·OH is the minor reactive species. According to the CB in 4%NBO whose reduced potential is lower than that of ·O₂[−]/O₂ (−0.33 eV) [74], it is possible that the photo-generated electrons can react with the adsorbed O₂ on the surface of 4%NBO, leading the mineralization of RhB in aqueous solution. The VB position (+0.87 eV) of 4%NBO is higher than that of ·OH/OH[−] (+2.27 eV) [75], so it couldn't form ·OH by the reaction of holes on 4%NBO nanosheets and H₂O. It should be mentioned that, for pure BiO_{2-x}, it couldn't generate the ·O₂[−] under NIR light irradiation, while the 4%NBO nanosheets possess the molecular activation ability to generate ·O₂[−] in the same conditions [52]. The characteristic signals of the DMPO-·O₂[−] can be obviously detected under UV-vis light irradiation for BiO_{2-x} and 4%NBO, and the 4%NBO reveals improved molecular oxygen activation (Fig. 10(b)). While, the characteristic signals of the DMPO-·O₂[−] can only observed with the addition of 4%NBO under NIR light irradiation. Besides, the signals of

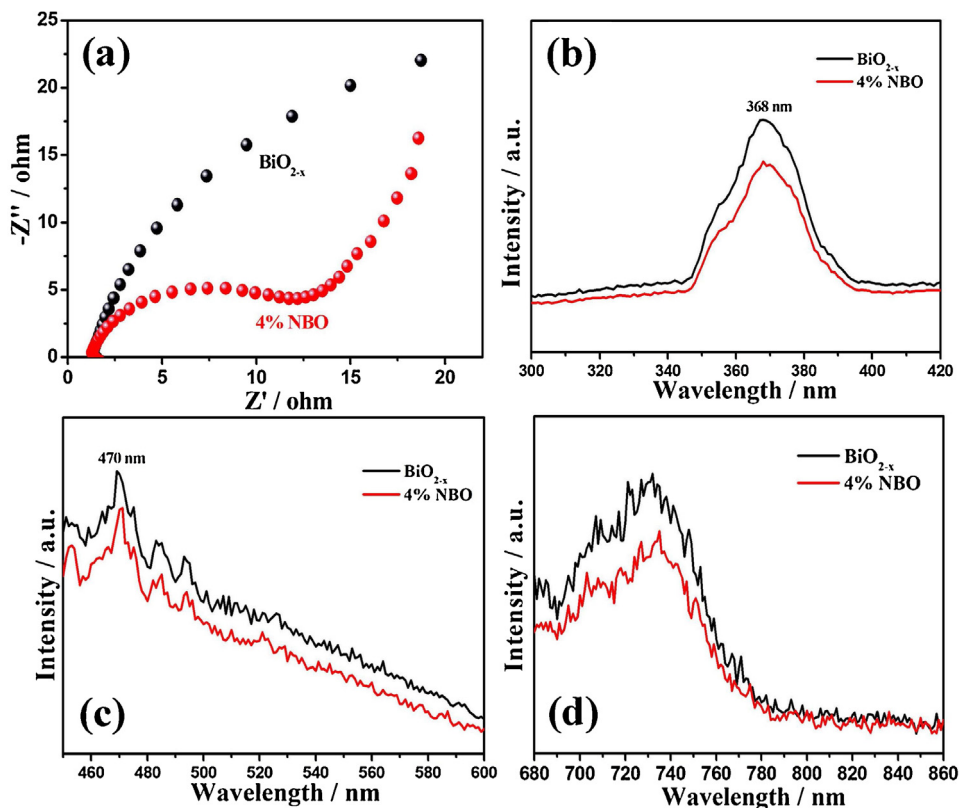


Fig. 9. (a) The EIS-Nyquist plot and (b–d) the photoluminescence (PL) spectra of BiO_{2-x} nanosheets and 4%NBO nanosheets.

the DMPO- $\cdot\text{OH}$ cannot be viewed under UV-vis or NIR irradiation. Considering the VB and CB potentials of BiO_{2-x} and 4%NBO, the enhanced UV, visible and NIR driven molecular oxygen activation into $\cdot\text{O}_2^-$ by 4%NBO could be mainly attributed to the introduction of Ni^{2+} .

3.10. Theoretical calculation

To better understand mechanisms of Ni^{2+} modification, molecular oxygen activation and charge behavior over Ni^{2+} doped BiO_{2-x} , DFT calculations were carried out. The crystal structure of Ni^{2+} -doped BiO_{2-x} was built by replacing a Bi atom with Ni atom in the primitive optimized cell of BiO_{2-x} to investigate the effect of doped Ni on the geometric and electronic structure of BiO_{2-x} (Fig. 11(a–b)). The results reveal that the cell parameters of the BiO_{2-x} and Ni^{2+} -doped BiO_{2-x} have a little difference (Table S1). Besides, after introducing Ni atom, the distance between Ni and neighboring oxygen atoms is shortened.

The calculation results show that the doped Ni atoms tend to approach the coordinated oxygen atoms, resulting in the formation of a distorted structure of Ni^{2+} -doped BiO_{2-x} . Fig. 11(c–d) revealed the total density of states (TDOS) and partial density of states (PDOS) of the element for Bi, O and Bi, Ni, O of BiO_{2-x} and Ni^{2+} -doped BiO_{2-x} , respectively. It is apparent that introducing Ni^{2+} results in the formation of a new doping energy level band. In this case, the photo-generated electrons could be easily excited into the doping energy level, which could be ascribed to the hybridization of d-orbital of Ni atoms and p-orbital of O atoms, and the resulting modification of electronic structure is responsible for enhanced photocatalytic activity of Ni^{2+} -doped BiO_{2-x} for degradation of RhB in aqueous solution.

To confirm the effect of Ni^{2+} on the molecular oxygen activation, we analyzed the differences in spatial charge distribution of BiO_{2-x} and Ni^{2+} -doped BiO_{2-x} after adsorbing O_2 , respectively (Fig. 12(a,b)). Because the Bi and Ni atoms belong to inhomogeneity, they exert distinct

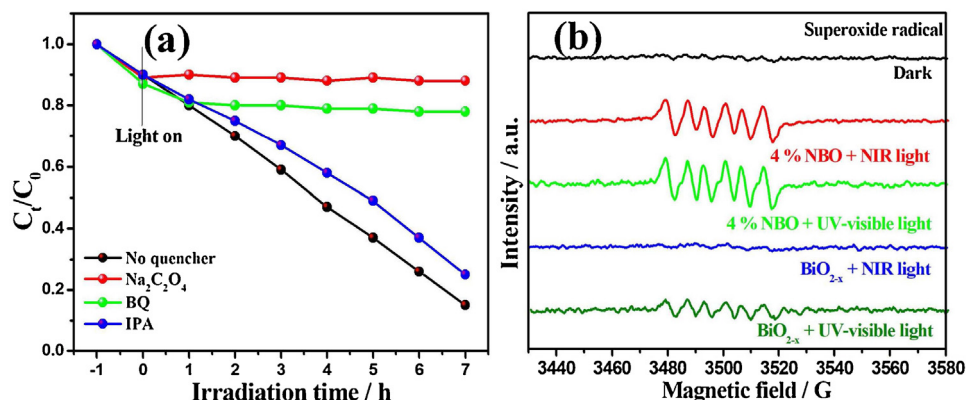


Fig. 10. (a) Photocatalytic degradation of RhB in aqueous solution over 4%NBO nanosheets with or without the quencher under NIR light irradiation. ESR signals of the (b) DMPO- $\cdot\text{O}_2^-$ for BiO_{2-x} and 4%NBO for 5 min under UV-vis and NIR irradiation, respectively.

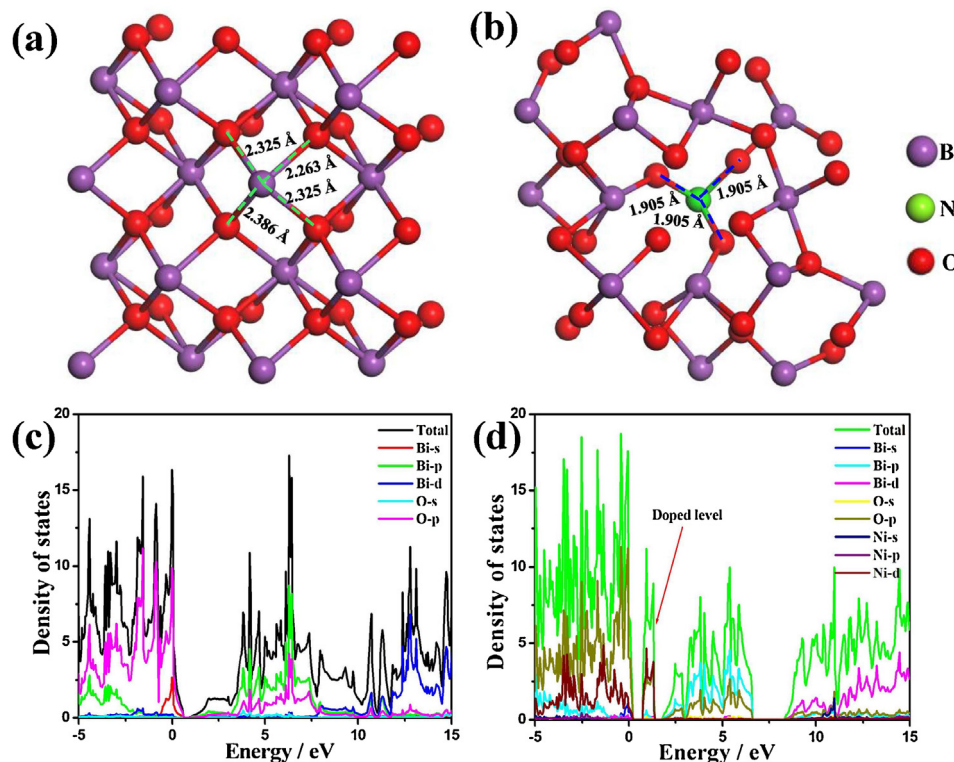


Fig. 11. DFT calculations. Crystal structures of (a) pristine $\text{BiO}_{2-\text{x}}$ and (b) Ni^{2+} -doped $\text{BiO}_{2-\text{x}}$; the density of states (DOS) of the (c) pristine $\text{BiO}_{2-\text{x}}$ and (d) Ni^{2+} -doped $\text{BiO}_{2-\text{x}}$.

influence on the charge distribution property for molecular oxygen activation. For the pure $\text{BiO}_{2-\text{x}}$, valence electrons are preferable to locate at O atoms for its stronger electrophilicity than Bi atom, which results in the formation of O anion. When Ni atom is introduced, forming a funnel like three-dimensional structure, the outermost electrons tend to accumulate on oxygen molecules adsorbed on the surface of Ni^{2+} -doped $\text{BiO}_{2-\text{x}}$, which attributes to achieve the activation of O_2 into $\cdot\text{O}_2^-$.

3.11. Photocatalytic mechanism of Ni^{2+} -doped $\text{BiO}_{2-\text{x}}$

Based on the above experimental and theoretical results, the photocatalytic mechanism of Ni^{2+} -doped $\text{BiO}_{2-\text{x}}$ for degradation of RhB in aqueous solution was schematically presented in Fig. 13. Under the irradiation of UV, visible and NIR light, firstly, the photo-excited electrons in Ni^{2+} -doped $\text{BiO}_{2-\text{x}}$ structure would transfer into the CB from the VB of Ni^{2+} -doped $\text{BiO}_{2-\text{x}}$ with completing the separation of electrons and holes. Secondly, the electrons transferred into the doped Ni^{2+} , subsequently transferring to the O_2 adsorbed on the surface of Ni^{2+} -doped $\text{BiO}_{2-\text{x}}$. Meanwhile, the photo-induced holes stay behind.

And then, the photo-excited electrons reacted with the O_2 adsorbed on Ni^{2+} -doped $\text{BiO}_{2-\text{x}}$ producing the $\cdot\text{O}_2^-$. The $\cdot\text{O}_2^-$ and holes would attack the RhB molecule, resulting in its mineralization into CO_2 , H_2O and other products. The self-interspersed nanosheet morphology of Ni^{2+} -doped $\text{BiO}_{2-\text{x}}$ with increased light-harvesting ability because of the multiple reflections of the incident light, also played a vital role in enhancing its photocatalytic activity. Therefore, the Ni^{2+} -doped $\text{BiO}_{2-\text{x}}$ nanosheets can serve as an attractive and promising full spectrum responsive photocatalyst.

4. Conclusions

The highly efficient Ni^{2+} -doped $\text{BiO}_{2-\text{x}}$ nanosheet photocatalysts with the UV, visible and NIR light-driven property were synthesized via a facile hydrothermal method. The introduction of Ni^{2+} source could reduce the reaction barrier and facilitate the formation of $\text{BiO}_{2-\text{x}}$. The Ni^{2+} -doped $\text{BiO}_{2-\text{x}}$ nanosheets exhibited enhanced photocatalytic activity in removal of RhB in aqueous solution under UV, visible and NIR light irradiation than pure $\text{BiO}_{2-\text{x}}$ nanosheets. The enhanced photocatalytic performance of Ni^{2+} -doped $\text{BiO}_{2-\text{x}}$ nanosheets could be

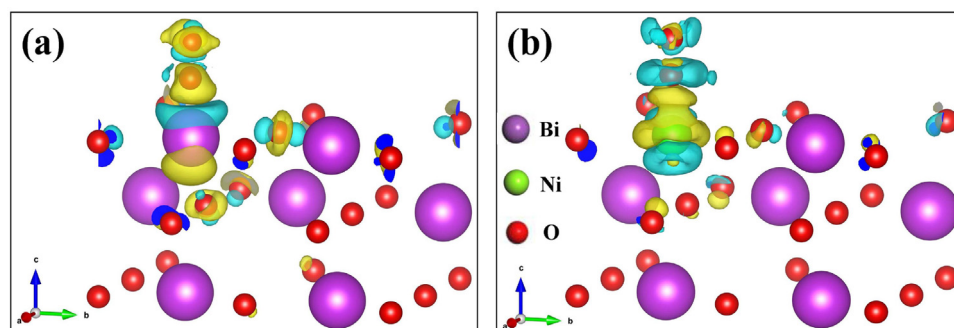


Fig. 12. Charge difference distribution of (a) $\text{BiO}_{2-\text{x}}$ and (b) Ni^{2+} -doped $\text{BiO}_{2-\text{x}}$ after adsorbing O_2 , respectively.

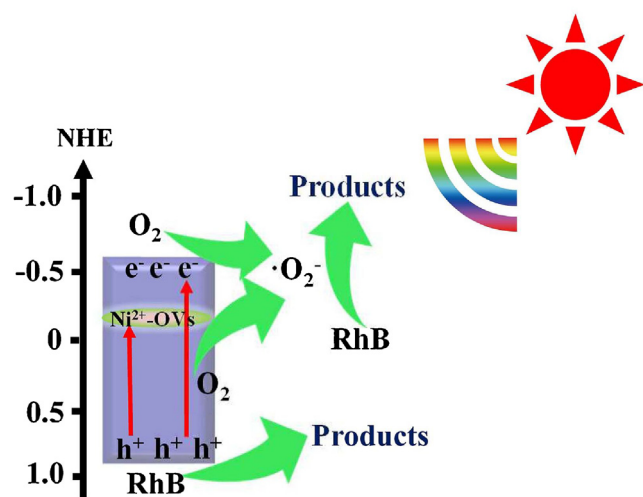


Fig. 13. Proposed mechanism for the NIR light photo-degradation of RhB and the effect on the electronic separation efficiency of Ni^{2+} -OVs over 4%NBO nanosheets.

ascribed to the synergistic effect of doping Ni^{2+} and OVs. The Ni^{2+} -doped in BiO_{2-x} could behave as the doping energy level to increase the potentials of its CB positions, to accelerate the separation efficiency of photo-generated carriers, resulting in the improved full spectrum driven molecular oxygen activation ability of Ni^{2+} -doped BiO_{2-x} , especially its NIR responsive molecular oxygen activation ability. Our study not only demonstrate the doping Ni^{2+} can facilitate the formation of BiO_{2-x} nanosheets and enhance the molecular oxygen activation ability of Ni^{2+} -doped BiO_{2-x} , but also provide a promising routine for developing highly efficient UV, visible and NIR responsive photocatalysts.

Acknowledgements

This work was supported by NSFC (No. 51472194), the NSF of Hubei Province (2016CFA078) and National Program on Key Basic Research Project of China (973 Program) 2013CB632402.

Appendix A. Supplementary data

Supplementary material related to this article can be found, in the online version, at doi:<https://doi.org/10.1016/j.apcatb.2018.04.016>.

References

- [1] A. Fujishima, K. Honda, *Nature* 238 (1972) 37–38.
- [2] Z.G. Xiong, X.S. Zhao, *J. Am. Chem. Soc.* 134 (2012) 5754–5757.
- [3] C.C. Chen, W.H. Ma, J.C. Zhao, *Chem. Soc. Rev.* 39 (2010) 4206–4219.
- [4] K. Mori, T. Taga, H. Yamashita, *ACS Catal.* 7 (2017) 3147–3151.
- [5] K. Wang, G.K. Zhang, J. Li, Y. Li, X.Y. Wu, *ACS Appl. Mater. Interfaces* 9 (2017) 43704–43715.
- [6] X.C. Wang, K. Maeda, A. Thomas, K. Takanabe, Xin G, J.M. Carlsson, K. Domen, M. Antonietti, *Nat. Mater.* 8 (2008) 76–80.
- [7] H.B. Yin, Y. Kuwahara, K. Mori, H.F. Cheng, M.C. Wen, H. Yamashita, *J. Mater. Chem. A* 5 (2017) 8946–8953.
- [8] H. Li, J. Shang, Z.H. Ai, L.Z. Zhang, *J. Am. Chem. Soc.* 137 (2015) 6393–6399.
- [9] D.D. Tang, J. Li, G.K. Zhang, *Appl. Catal. B: Environ.* 224 (2018) 433–441.
- [10] X. Hai, W. Zhou, S.Y. Wang, H. Pang, K. Chang, F. Ichihara, J.H. Ye, *Nano Energy* 39 (2017) 409–417.
- [11] L.C. Liu, X.R. Gu, Z.Y. Ji, W.X. Zou, C.J. Tang, F. Gao, L. Dong, *J. Phys. Chem. C* 117 (2013) 18578–18587.
- [12] M.Y. Xing, B.C. Qiu, M.M. Du, Q.H. Zhu, L.Z. Wang, J.L. Zhang, *Adv. Funct. Mater.* 27 (2017) 1702624.
- [13] M.Y. Xing, J.L. Zhang, B.C. Qiu, B.Z. Tian, M. Anpo, M. Che, *Small* 11 (2015) 1920–1929.
- [14] X. Ding, W.K. Ho, J. Shang, L.Z. Zhang, *Appl. Catal. B: Environ.* 182 (2016) 316–325.
- [15] G.S. Li, Z.C. Lian, X. Li, Y.Y. Xu, W.C. Wang, D.Q. Zhang, F.H. Tian, H.X. Li, *Appl. Catal. B: Environ.* 3 (2015) 3748–3756.
- [16] Y. Zhou, Y.C. Liu, P.W. Liu, W.Y. Zhang, M.Y. Xing, J.L. Zhang, *Appl. Catal. B: Environ.* 170 (2015) 66–73.
- [17] G.X. Zhu, J.G. Zhu, W.J. Jiang, Z.J. Zhang, J. Wang, Y.F. Zhu, Q.F. Zhang, *Appl. Catal. B: Environ.* 209 (2017) 729–737.
- [18] J.F. Xie, H. Zhang, S. Li, R.X. Wang, X. Sun, M. Zhou, J.F. Zhou, X.W. Lou, Y. Xie, *Adv. Mater.* 25 (2013) 5807–5813.
- [19] D.D. Tang, G.K. Zhang, *Appl. Surf. Sci.* 391 (2017) 415–422.
- [20] Z. Wan, G.K. Zhang, X.Y. Wu, S. Yin, *Appl. Catal. B: Environ.* 207 (2017) 17–26.
- [21] W.X. Zou, Y. Shao, Y. Pu, Y.D. Luo, J.F. Sun, K.L. Ma, C.J. Tang, F. Gao, L. Dong, *Appl. Catal. B: Environ.* 218 (2017) 51–59.
- [22] W.X. Zou, L. Zhang, L.C. Liu, X.B. Wang, J.F. Sun, S.G. Wu, Y. Deng, C.J. Tang, F. Gao, L. Dong, *Appl. Catal. B: Environ.* 181 (2016) 495–503.
- [23] L.C. Liu, Z.Y. Ji, W.X. Zou, X.R. Gu, Y. Deng, F. Gao, C.J. Tang, L. Dong, *ACS Catal.* 3 (2013) 2052–2061.
- [24] L. Pan, J.J. Zou, X.W. Zhang, L. Wang, *J. Am. Chem. Soc.* 133 (2011) 10000–10002.
- [25] H.W. Huang, R.R. Cao, S.X. Yu, K. Xu, W.C. Hao, Y.G. Wang, F. Dong, T.R. Zhang, Y.H. Zhang, *Appl. Catal. B: Environ.* 219 (2017) 526–537.
- [26] M.S. Zhu, X.Y. Cai, M. Fujitsuka, J.Y. Zhang, T. Majima, *Angew. Chem. Int. Ed.* 56 (2017) 2064–2068.
- [27] Y. Ma, X.Y. Wu, G.K. Zhang, *Appl. Catal. B: Environ.* 205 (2017) 262–270.
- [28] C.D. Lv, G. Chen, X. Zhou, C.M. Zhang, Z.K. Wang, B.R. Zhao, D.Y. Li, *ACS Appl. Mater. Interfaces* 9 (2017) 23748–23755.
- [29] T. Xiong, W.L. Cen, X.Y. Zhang, F. Dong, *ACS Catal.* 6 (2016) 2462–2472.
- [30] G. Liu, L.C. Yin, J.Q. Wang, P. Niu, C. Zhen, Y.P. Xie, H.M. Cheng, *Energy Environ. Sci.* 5 (2012) 9603–9610.
- [31] B. Zhang, H.P. Zhang, Z.Y. Wang, X.Y. Zhang, X.Y. Qin, Y. Dai, Y.Y. Liu, P. Wang, Y.J. Li, B.B. Huang, *Appl. Catal. B: Environ.* 211 (2017) 258–265.
- [32] X.S. Nguyen, G.K. Zhang, X.F. Yang, *ACS Appl. Mater. Interfaces* 9 (2017) 8900–8909.
- [33] H. Zhang, Z.P. Xing, Y. Zhang, Z.Z. Li, X.Y. Wu, C.T. Liu, Q. Zhu, W. Zhou, *RSC Adv.* 5 (2015) 107150–107157.
- [34] G.Y. Zhu, L.B. Ma, H.L. Lv, Y. Hu, T. Chen, R.P. Chen, J. Liang, X. Wang, Y.R. Wang, C.Z. Yan, Z.X. Tie, Z. Jin, J. Liu, *Nanoscale* 9 (2017) 1237–1243.
- [35] X.Y. Wu, S. Yin, Q. Dong, T. Sato, *Appl. Catal. B: Environ.* 156 (2014) 257–264.
- [36] C.H. Li, F. Wang, J. Zhu, J.C. Yu, *Appl. Catal. B: Environ.* 100 (2010) 433–439.
- [37] Z.J. Zhang, W.Z. Wang, *Dalton Trans.* 42 (2013) 12072–12074.
- [38] J.J. Wang, L. Tang, G.M. Zeng, Y.C. Deng, H.R. Dong, Y.N. Liu, L.L. Wang, B. Peng, C. Zhang, F. Chen, *Appl. Catal. B: Environ.* 222 (2018) 115–123.
- [39] D. Wei, L.H. Yao, S. Yang, Z.T. Cui, B.X. Wei, M.H. Cao, C.W. Hu, *ACS Appl. Mater. Interfaces* 7 (2015) 20761–20768.
- [40] X.L. Hu, Y.Y. Li, J. Tian, H.R. Yang, H.Z. Cui, *J. Ind. Eng. Chem.* 45 (2017) 189–196.
- [41] G.W. Cui, W. Wang, M.Y. Ma, J.F. Xie, X.F. Shi, N. Deng, J.P. Xin, B. Tang, *Nano Lett.* 15 (2015) 7199–7203.
- [42] T. Jing, Y. Dai, W. Wei, X.C. Ma, B.B. Huang, *Phys. Chem. Chem. Phys.* 16 (2014) 18596–18604.
- [43] G. Wang, B.B. Huang, X.C. Ma, Z.Y. Wang, X.Y. Qin, X.Y. Zhang, Y. Dai, M.H. Whangbo, *Angew. Chem. Int. Ed.* 52 (2013) 4810–4813.
- [44] W. Jiang, X.Y. Wang, Z.W. Wu, X.N. Yue, S.J. Yuan, H.F. Lu, B. Liang, *Ind. Eng. Chem. Res.* 54 (2015) 832–841.
- [45] J. Tian, Y.H. Sang, G.W. Yu, H.D. Jiang, X.N. Mu, H. Liu, *Adv. Mater.* 25 (2013) 5075–5080.
- [46] R.A. He, S.W. Cao, P. Zhou, J.G. Yu, *Chin. J. Catal.* 35 (2014) 989–1007.
- [47] Z. Wan, G.K. Zhang, *J. Mater. Chem. A* 3 (2015) 16737–16745.
- [48] C.L. Yu, Z. Wu, R.Y. Liu, D.D. Dionysiou, K. Yang, C.Y. Wang, H. Liu, *Appl. Catal. B: Environ.* 209 (2017) 1–11.
- [49] Y.Y. Liu, Z.Y. Wang, B.B. Huang, K.S. Yang, X.Y. Zhang, X.Y. Qin, Y. Dai, *Appl. Surf. Sci.* 257 (2010) 172–175.
- [50] X. Zhang, Z.H. Ai, F.L. Jia, L.Z. Zhang, *J. Phys. Chem. C* 112 (2008) 747–753 112.
- [51] L.Q. Ye, J.Y. Liu, C.Q. Gong, L.Q. Tian, T.Y. Peng, L. Zan, *ACS Catal.* 2 (2012) 1677–1683.
- [52] J. Li, X.Y. Wu, W.F. Pan, G.K. Zhang, H. Chen, *Angew. Chem. Int. Ed.* 57 (2018) 491–495.
- [53] S.N. Zhang, S.J. Zhang, L.M. Song, *Appl. Catal. B: Environ.* 152 (2014) 129–139.
- [54] S.J. Zhu, L.L. Lu, Z.W. Zhao, T. Wang, X.Y. Liu, H.J. Zhang, F. Dong, Y.X. Zhang, J. Phys. Chem. C 121 (2017) 9394–9401.
- [55] Y.B. Ding, F. Yang, L.H. Zhu, N. Wang, H.Q. Tang, *Appl. Catal. B: Environ.* 164 (2015) 151–158.
- [56] N. Singh, J. Prakash, M. Misra, A. Sharma, R.K. Gupta, *ACS Appl. Mater. Interfaces* 9 (2017) 28495–28507.
- [57] G.D. Tang, X.Q. Shi, C. Huo, Z.H. Zhang, *Ceram. Int.* 39 (2013) 4825–4829.
- [58] T.J. Lin, H. Xie, X. Meng, L. Shi, *Catal. Commun.* 68 (2015) 88–92.
- [59] D. Yan, C.Y. Yu, D.S. Li, X.J. Zhang, J.B. Li, T. Lu, L.K. Pan, J. Mater. Chem. A 4 (2016) 11077–11085.
- [60] Y.K. Huang, S.F. Kang, Y. Yang, H.F. Qin, Z.J. Ni, S.J. Yang, X. Li, *Appl. Catal. B: Environ.* 196 (2016) 89–99.
- [61] Y.F. Sun, S. Gao, F.C. Lei, Y. Xie, *Chem. Soc. Rev.* 44 (2015) 623–636.
- [62] X.D. Meng, G.K. Zhang, N. Li, *Chem. Eng. J.* 314 (2017) 249–256.
- [63] N. Yavo, A.D. Smith, O. Yeheskel, S. Cohen, R. Korobko, E. Wachtel, P.R. later, I. Lubomirsky, *Adv. Funct. Mater.* 26 (2016) 1138–1142.
- [64] A. Dapčević, D. Poleti, J. Rogan, A. Radojković, M. Radović, G. Branković, 280 (2015) 18–23.
- [65] X.P. Lin, F.Q. Huang, W.D. Wang, J.L. Shi, *Scripta Mater.* 56 (2007) 189–192.
- [66] Y.H. Lv, Y.Y. Zhu, Y.F. Zhu, *J. Phys. Chem. C* 117 (2013) 18520–18528.
- [67] G.S. Li, Z.C. Lian, X. Li, Y.Y. Xu, W.C. Wang, D.Q. Zhang, F.H. Tian, H.X. Li, *J. Mater. Chem. A* 3 (2015) 3748–3756.
- [68] R. Li, Q. Zhen, M. Drache, A. Rubbens, C. Estournes, R.N. Vannier, *Solid State Ionics*

- 198 (2011) 6–15.
- [69] B.X. Li, X.K. Shao, T.X. Liu, L.Z. Shao, B.S. Zhang, *Appl. Catal. B: Environ.* 198 (2016) 325–333.
- [70] D. Maruthamani, D. Divakar, M. Kumaravel, *J. Ind. Eng. Chem.* 30 (2015) 33–43.
- [71] X.Y. Wu, M.M. Li, J. Li, G.K. Zhang, S. Yin, *Appl. Catal. B: Environ.* 219 (2017) 132–141.
- [72] J.D. Li, X.L. Zhang, F. Raziq, J.S. Wang, C. Liu, Y. Liu, J.W. Sun, R. Yan, B.H. Qu, C.L. Qin, L.Q. Jing, *Appl. Catal. B: Environ.* 218 (2017) 60–67.
- [73] D.J. Mao, S.S. Ding, L.J. Meng, Y.X. Dai, C. Sun, S.G. Yang, H. He, *Appl. Catal. B: Environ.* 207 (2017) 153–165.
- [74] P. Zhou, J.G. Yu, M. Jaroniec, *Adv. Mater.* 26 (2014) 4920–4935.
- [75] H.W. Huang, Y. He, X.W. Li, M. Li, C. Zeng, F. Dong, X. Du, T.R. Zhang, Y.H. Zhang, *J. Mater. Chem. A* 3 (2015) 24547–24556.